05,08,10,11

Selection of ferromagnetic nanoparticles in the process of synthesis of perfect and defective carbon nanotubes by a catalytic method

© E.I. Kunitsyna[1,2], A.D. Talantsev[1], E.V. Dvoretskaya[1], V.V. Savin[22], R.B. Morgunov[1,2,3,¶]

[1] Federal Research Center of Problems of Chemical Physics and Medicinal Chemistry RAS, Chernogolovka, Russia
[2] Immanuel Kant Baltic Federal University, Kaliningrad, Russia
[3] Tambov State Technical University, Tambov, Russia

¶E-mail: spintronics2022@yandex.ru

Received November 21, 2025
Revised November 21, 2025
Accepted November 23, 2025

It was found that nanotubes with defects contain larger core-shell Fe/Fe_3O_4 particles with a higher coercive force than perfect nanotubes, but the relative proportion of such particles is 4 times smaller in defective nanotubes, all other conditions being equal (growth rate in butanol, temperature).

Keywords: core–shell particles, nanocomposites, Raman spectroscopy, chemical vapor deposition, carbon nanotube fibers.

DOI: 10.61011/PSS.2025.11.62962.329-25

1. Introduction

Carbon nanotubes (CNTs) are one of the most promising classes of nanostructures due to their outstanding electric, thermal, mechanical and structural properties. In particular, the capacity of CNTs for high conductivity, considerable specific surface makes them attractive for a wide spectrum of applications — from composite materials and electrodes to sensors and magnetic systems [1,2].

Recently the attention of the researchers shifted towards the CNT modification by inclusion of metal particles into a reaction mixture when growing nanotubes [3–5]. This makes it possible to integrate magnetic, catalytic and/or ferromagnetic functions of nanoparticles into a carbon matrix. CNTs containing ferromagnetic metal nanoparticles are interesting since they may perform the following functions: 1) be markers of nanotubes, making it possible to judge the local environment of particles by measurements of magnetic properties of the material and to identify the variation of the latter in different processes, 2) modify nanotubes, defining the conditions for their growth, in particular, diameter and layering, 3) create conditions for proximity effects, providing for the magnetic ordering of defect spins in nanotubes as such, 4) act as magnetically active components that manage CNT conductivity in magnetization of nanoparticles. Such systems are attractive for magnetic nano-composites, recording devices, magnetic control or catalysis with magnetic separation [6,7].

Since the magnetism of the carbon systems is always related to the presence of defects therein, which either result in broken carbon bonds or are the defects of magnetic impurity, you can expect that the interaction of the perfect CNTs and the nanotubes with defects with metal ferromagnetic nanoparticles will differ, changing the statistics of nanotube decoration with nanoparticles. In this paper the focus is on the identification of the role of defects in CNTs for the magnetic properties of the ensemble of nanoparticles associated with carbon nanotubes.

It may turn out that the presence of ferromagnetic particles also affects the CNT growth. In the context of growth and treatment of CNTs, it is important to note that the control of morphology, the number of walls, diameter and length of tubes remains critical for the achievement of high functional characteristics. In papers [8,9] it is shown that you can control the type of CNTs (single-wall/multi-wall) upon production, varying the ratio of precursor concentration and catalyst, and also the reaction temperature. Therefore, we controlled the degree of defectiveness and layering of CNTs using Raman-scattering spectroscopy.

The purpose of this paper is to identify the effect of nanotube formation speed on the obtained dimensions of ferrous doping particles and magnetic properties of CNT fibers.

2. Methodology and samples

Fibers of carbon nanotubes were synthesized in the laboratory by the method of chemical deposition from the vapor phase of the floating catalyst [8,9] in a laboratory reactor of vertical configuration with inner diameter of 70 mm and introduction of precursors at the top. The reactor was equipped with a mullite tube-type furnace. This is a single-stage method of gas phase synthesis, in which the assembly of very long CNTs causes their entanglement as they are

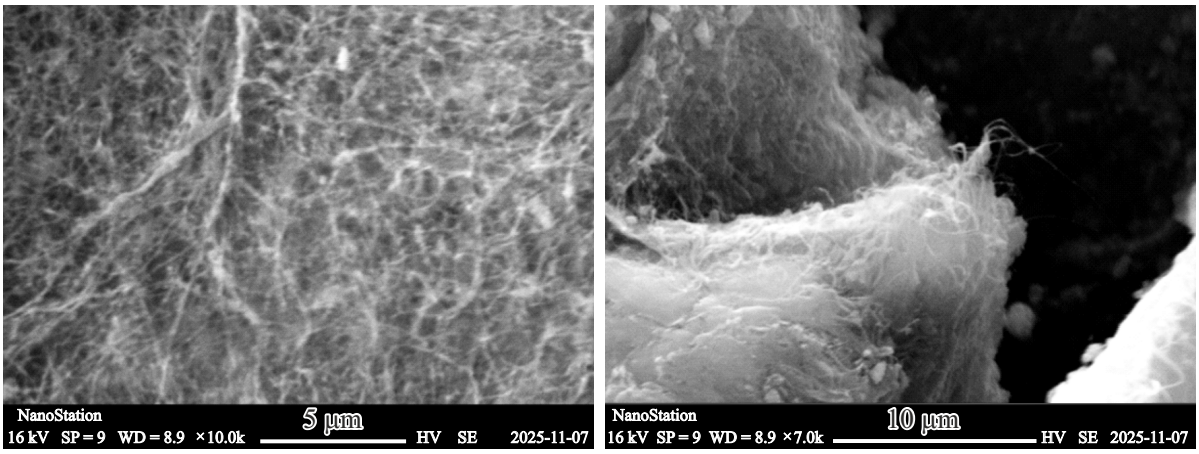

Figure 1. Images of *1* sample fibers obtained using SEM.

growing, forming an aerogel, which is then drawn from the reactor and is wound on the coil.

The precursors were introduced via an injector tube with outer diameter of 1.5 mm and inner diameter of 0.1 mm for toluene (or butanol) and ferrocene solution, and also with outer diameter 6 mm and inner diameter of 4 mm for evaporated sulfur, which then exited through the reactor tube flange at temperature of 100 °C.

In this paper the furnace was heated to temperature of 1300 °C. The synthesis conditions were selected for the study of various atomic ratio of sulfur and carbon, whereas other parameters, such as speed of injection, hydrogen consumption etc., were maintained permanent. CNT aerogel was extracted at the exit from the reactor and continuously collected on a spool rotating with the speed of 30–140 rpm, which corresponded to the speeds of fiber formation of 6–28 m/min. The precise time of collection of all samples was recorded with a stopwatch. Then the aerogel threads were condensed in autonomous mode (not removing them off the spool) using isopropyl alcohol and were left to dry for the night. The additional extension at the stages of collection and condensation was not applied, which maintained the internal orientation of the CNT bundles in the fibers. (To ensure the reproducibility, the CNT fiber samples obtained for the first hour of reactor operation were rejected.)

The paper compares two types of precursors: butanol and toluene. For CNTs obtained from toluene, by variation of the reaction temperature and S/C ratio, the model of stable fiber formation was selected, which remained stable with temperature rise. For CNTs obtained on the basis of butanol, the increase of the reaction temperature caused unstable fiber formation. For both types of materials the drawing speed was close to the optimal from the point of view of longitudinal properties and simplicity of manufacturing.

The process of carbon nanotube formation may be described using the theory of thermodynamic equilibrium of phases, according to which the nucleation of a nanowire is presented in the form of a trajectory in the isothermal phase diagram, starting from the end of the catalyst and moving towards the nanowire components. A triple diagram Fe–S–C at high temperature is an iron-rich liquid (L) and two non-mixing liquids, one of which is rich in carbon (L_1), and the other one — in sulfide (L_2). At high content of carbon the non-mixing liquids are in equilibrium with solid carbon ($L_1+L_2+C(s)$). Presumably, CNTs grow at lower content of sulfur at the interface L and L_1+L_2, where solid carbon is not in the equilibrium and, accordingly, is ejected as side walls of CNT. Formation of a shell containing sulfur is predicted with a phase diagram in cooling and is observed experimentally. In previous works it was shown for such doped CNTs that the higher the S/C ratio, the more the number of walls in each CNT. At S/C concentration of 0.01%, single-wall CNTs are observed, which are grouped together. Increase of S/C increases the number of layers from 1 to 8 and reduces the average length from 34 to 6 μm.

The paper studies five samples: No. *1* and *2* — precursor: butanol, formation speeds 6 and 20 m/min accordingly, No. *3–5* — precursor: toluene, formation speeds 7, 14 and 28 m/min accordingly.

The typical image of fiber comprising nanotubes is shown in Figure 1 for sample *1* with different magnification of scanning electron microscope (SEM).

The optical properties were studied using a Raman scattering spectrophotometer Confotec NR500 with a laser at wavelength of 532 nm, lens ×40 and lens Horiba LabRAM ×100, lattices 600 line/mm, laser capacity 50 mW. The spectra were averaged in three–five measurements recorded from different areas of the sample to get an idea of the spread. The spectrum recording time was 300 s. Magnetic measurements were performed using the SQUID MPMS 5XL Quantum Design magnetometer in the temperature range from 2 to 300 K and in magnetic field from 0 to 50 kOe.

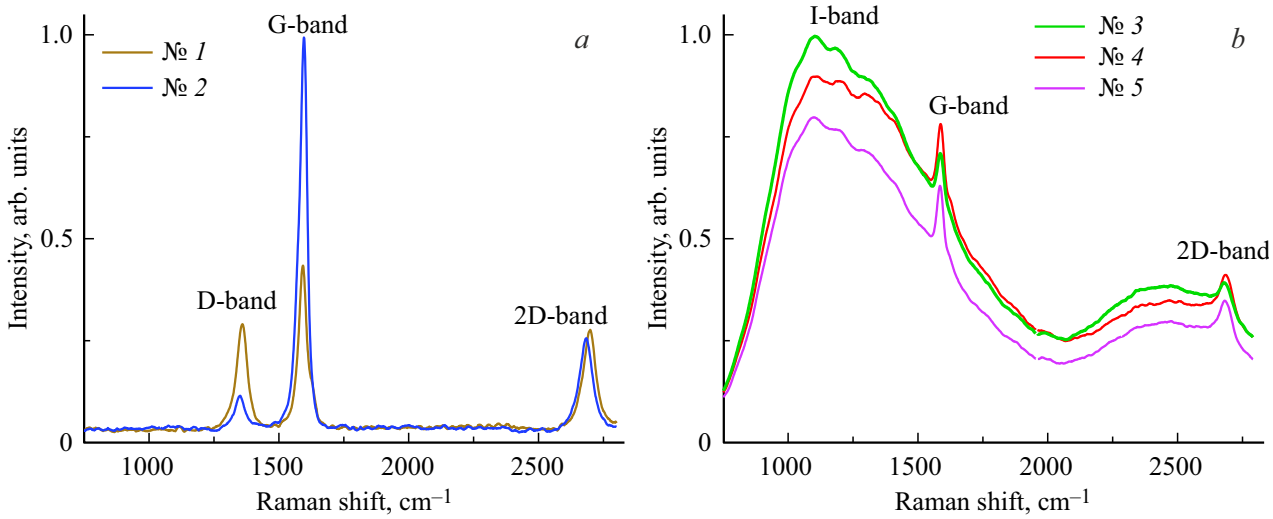

Figure 2. Raman spectra of samples obtained using as a precursor *a*) of butanol in samples *1* and *2* and *b*) toluene in samples *3*–*5*.

Table 1. Positions and widths at half maximum for maxima of Raman spectra of samples *1*–*5*

No. of sample	D-peak		G-peak		2D-peak	
	Max, cm^{-1}	FWHM, cm^{-1}	Max, cm^{-1}	FWHM, cm^{-1}	Max, cm^{-1}	FWHM, cm^{-1}
1	1360	45	1592	34	2700	56
2	1349	42	1598	33	2682	54
3	–		1593	30	2692	65
4	–		1593	32	2695	66
5	–		1590	31	2695	66

3. Experimental results and discussion

3.1. Raman spectroscopy

Figure 2 shows the Raman scattering spectra of samples with different types of precursors: butanol (Figure 2, *a*) and toluene (Figure 2, *b*).

Table 1 shows the positions of the peak maxima D, G and 2D (Max), and their width at half maximum (FWHM) for all samples *1*–*5*.

Three peaks are available in the spectra of the samples obtained using butanol (see Table 1). Ratio of maximum amplitudes for sample *1*: $J_D/J_G = 0.62$, $J_{2D}/J_D = 0.96$, for sample *2*: $J_D/J_G = 0.08$, $J_{2D}/J_D = 2.83$.

You can see that the samples grown in butanol, *1* and *2*, are characterized with narrower peaks 2D and broadened peaks G compared to the peaks of samples *3*–*5*, grown in toluene.

The peak at $\sim 1350\,cm^{-1}$ is called a D-peak in the literature. It characterizes the disturbed sp^2-bonds in CNTs associated with defects. The sample *1* has a wider and more intense D-peak, which means that it has a higher concentration of defects and more functional groups compared to the sample *2*. G-peak (~ 1580–$1600\,cm^{-1}$), responsible for the ordering of the CNT structure, also demonstrates that the sample *2* has an improved structure. And, finally, 2D-peak ($\sim 2700\,cm^{-1}$) being an indicator of the number of the walls, in sample *2* is displaced to the smaller wavelengths ($2682\,cm^{-1}$), which is typical for single-wall or small-wall CNTs (see Table 1). In sample *1* the 2D peak is wider, which indicates the overlapping of signals from different walls (common for multi-wall CNTs or defective bundles of CNTs). You can assume that in sample *1* the share of single-wall CNTs does not exceed 40%, and in sample *2* the share of single-wall CNTs is 90–95%.

For all samples of toluene series, a wide double halo was observed with maxima at $1100\,cm^{-1}$ and $2500\,cm^{-1}$, which may indicate a high quantity of amorphous carbon („I-band“) or, less often, the strong modification of CNTs by foreign particles [10].

3.2. SQUID magnetometry

In Figure 3 the hysteresis loops are presented for magnetization M of *1* and it2 samples with a precursor: butanol at temperature of 300 K (Figure 3, *a*) and 2 K (Figure 3, *b*).

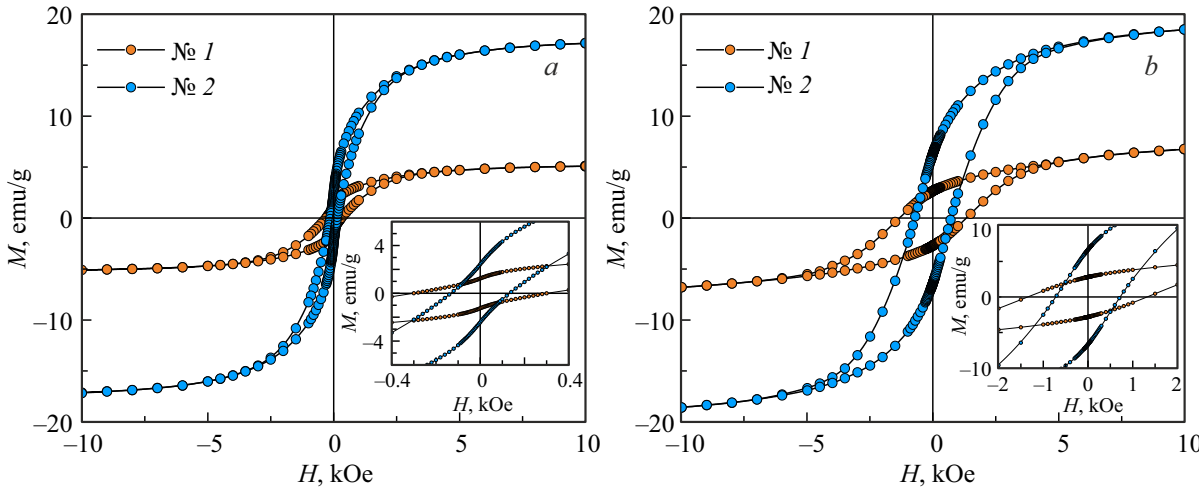

Figure 3. Dependences of magnetization on the field for samples *1* and *2*, obtained using butanol at *a*) 300 K and *b*) 2 K.

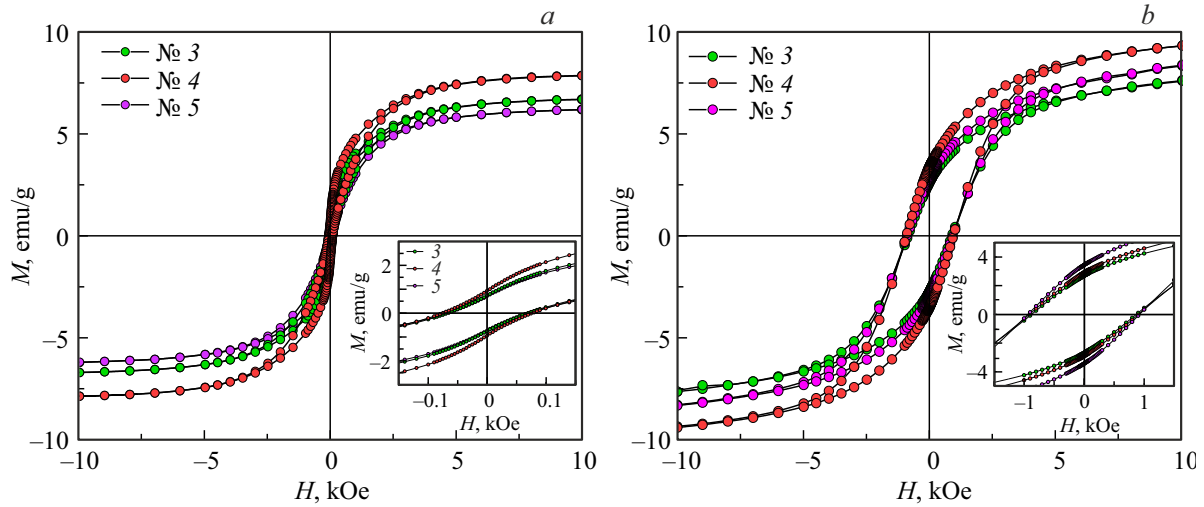

Figure 4. Dependences of magnetic torque on the field for samples *3*–*5*, obtained using toluene as precursor at *a*) 300 K and *b*) 2 K.

You can see that for samples produced with butanol precursor (Figure 3, *a*), strong dependence is observed between the coercive force and speed of fiber drawing: with growth of speed at ~ 3 times the sample *2* shows a double decrease of the coercive force and increase of the saturation magnetization $M_s \sim 3$ times. If you neglect the contribution of the oxidized shell and accept that the magnetizations of saturation of a ferrous nucleus in a nanoparticle at room temperature is $M_s(\mathrm{Fe}) \approx 200-220$ emu/g, then, taking into account the different magnetization of saturation of *1* and *2* samples, the weight content of iron therein will be ~ 2 and $\sim 8\%$ accordingly.

Figure 4 presents the hysteresis loops of samples *3*–*5*, obtained using toluene as a precursor, at *a*) 300 K and *b*) 2 K. The growth of magnetic anisotropy at decrease of temperature predictably causes increase of coercive force that does not depend on the speed of fiber drawing and is the same in all samples *3*–*5*. Magnetization of saturation depends on the fiber drawing speed in a non-monotonic nature.

Since the coercive force H_c for single-domain nanoparticles may be calculated using equation $H_c = 2K/M_s$, this makes it possible to compare the anisotropy constants K for all samples *1*–*5* (see Table 2).

In *1* and *2* samples the anisotropy constant K turns out considerably higher than in samples *3*–*5*, both at 300 K and at 2 K. Besides, K grows with the speed of fiber drawing in *1* and *2* samples and depends in a non-monotonic manner on this speed in samples *3*–*5*.

According to [11], at particle dimensions below the single-domain size limit, when the particle is remagnetized coherently in the magnetic field, its coercive force depends on volume V and diameter D according to the formula:

$$H_c = H_{c0}\left[1 - \left(\frac{V_{\mathrm{cr}}}{V}\right)^{1/2}\right] = H_{c0}\left[1 - \left(\frac{D_{\mathrm{cr}}}{D}\right)^{3/2}\right],$$

where V_{cr} — critical volume of the particle.

From this formula it follows that the coercive force grows with increase of the volume or diameter of single-domain

Table 2. Coercive force, magnetization of saturation, ratio of residual magnetization to magnetization of saturation M_r/M_s and estimated effective constant of anisotropy K of samples *1*–*5*

No. of sample	Speed formation, m/min	H_c, Oe		M_s, emu/g		K, 10^4 erg/cm^3		M_r/M_s	
		2 K	300 K	2 K	300 K	2 K	300 K	2 K	300 K
1	6	1320	300	9.85	5.77	5.12	0.68	0.285	0.215
2	20	720	135	22.95	18.12	6.51	0.96	0.290	0.134
3	7	880	70	10.23	6.74	3.54	0.19	0.262	0.111
4	14	930	76	11.30	7.62	4.14	0.23	0.305	0.123
5	28	900	70	11.09	6.43	3.93	0.18	0.264	0.111

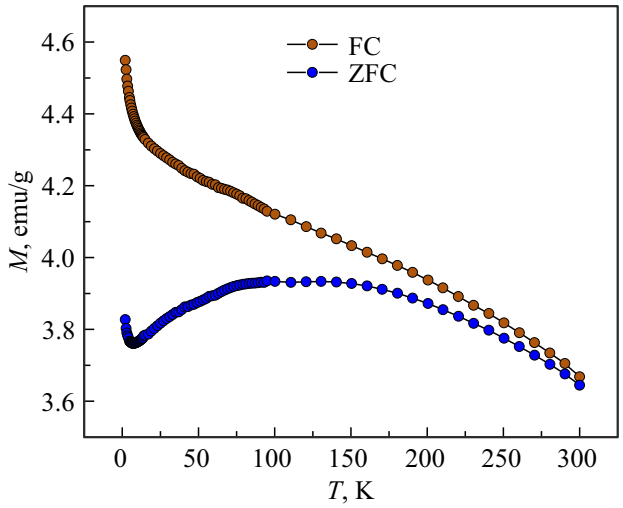

Figure 5. Dependences of sample *1* magnetization on temperature measured in sample heating in constant magnetic field 2 kOe, after sample cooling in magnetic field 1 T (FC) and after sample cooling in zero field (ZFC).

particles. Therefore, for particles in *1* and *2* samples, differing only with the fiber drawing speed, the decrease in the particle size may be assumed with the drawing speed as their quantity increases. The coercive force of samples *3*–*5*, on the contrary, did not depend on the fiber drawing speed (Figure 4), and therefore the particle dimensions were most probably constant. However, at the same time the saturation magnetization changed in a non-monotonic manner, which could have been related to both a change in the number of particles decorating the nanotubes and to variations of the oxidized layer thickness. In samples *3*–*5*, according to a wide halo in Raman spectra (Figure 2, *b*), there is a significant part of amorphous material, so that the drawing speed will hardly change the contribution to the perfect nanotubes present in a small proportion.

Figure 5 presents the dependences of sample *1* magnetization on temperature measured in sample heating in constant magnetic field 2 kOe, after sample cooling in magnetic field (field cooling, FC) 1 T and after sample cooling in zero field (zero field cooling, ZFC).

From these curves you may conclude that the blocking temperature T_b determined as the point of their crossing, is approximately equal to 300 K for sample *1*. The blocking temperature depends on the anisotropy constant of material K and their volume V: $T_b = K \cdot V/25k_B$ (k_B — Boltzmann constant) at one chart point measurement time is ~ 100 s. Since K is known from magnetization of saturation and coercive force (see Table 2), you may assess the volume of nanoparticle $V = 25k_BT_b/K = 1.5 \cdot 10^{-16}$ m^3, which corresponds to the diameter of nanoparticles ~ 10 Å. Since in [12] the average diameter of nanoparticles was determined experimentally using electron microscopy and amounted to not more than 60 Å, our estimate turns out to be very low. This error may be related to the substantial share of the oxide shell in nanoparticles, which is unknown, but iron oxide has substantially different magnetic anisotropy $K = 24.3 \cdot 10^4$ erg/cm^3 [13] compared to magnetic anisotropy of iron, which is in the nucleus of nanoparticles [14].

The detailed analysis of magnetic anisotropy of iron particles with diameter of 10–100 Å is given in [14] based on the comparison of the ratio of residual magnetization M_r to saturation magnetization M_s. It is noted that for non-interacting, randomly oriented uniaxial particles the ratio is $M_r/M_s \approx 0.5$ and increases to 0.8 with the presence of the cubic anisotropy. The ratio M_r/M_s below 0.5 (see Table 2) indicates the following: contribution of superparamagnetic particles, strong dipole interactions or heterogeneities of the shape (large proportion of surface oxide). Note that in sample *1* the ratio M_r/M_s practically does not change in the transition from 2 to 300 K (see Table 2), the contribution of superparamagnetic particles therein is minimal. Accordingly, the share of the superparamagnetic phase in sample *1* is lower than in samples *2*–*5*.

4. Conclusion

It was found that nanotubes with defects contain larger core-shell Fe/Fe_3O_4 particles with large coercive force

(2.2 times) compared to perfect nanotubes, however, at the same time the relative share of such particles is 4 times smaller in the defective nanotubes at other equal conditions (growth speed in butanol, temperature). The disordered mix of nanotubes with a significant share of amorphous carbon obtained in toluene demonstrates the same coercive force of Fe/Fe_3O_4 nanoparticles regardless of the carbon fiber drawing speed. Therefore, the carbon structures select and promote the elective growth of larger Fe/Fe_3O_4 particles in butanol. This effect is masked with the presence of the large share of amorphous phase of carbon when nanotubes are grown in toluene.

Acknowledgments

The authors are grateful to M. Vazquez-Pufleau from IMDEA Materials, Madrid, Spain, for the samples provided for research.

Funding

The study was carried out within the grant of the Russian Science Foundation No. 25-72-31032, https://rscf.ru/project/25-72-31032/.

Conflict of interest

The authors declare that they have no conflict of interest.

References

[1] K.J. Hughes, K.A. Iyer, R.E. Bird, J. Ivanov, S. Banerjee, G. Georges, Q.A. Zhou. ACS Appl. Nano Mater. **7**, *16*, 18695 (2024). https://doi.org/10.1021/acsanm.4c02721
[2] M. Syduzzaman, M.S. Islam Saad, M.F. Piam, T.A. Talukdar, T.T. Shobdo, N.M. Pritha. Results Mater. **25**, 100654 (2025). https://doi.org/10.1016/j.rinma.2024.100654
[3] T. Moriai, T. Tsukamoto, K. Fukuhara, T. Imaoka, T. Kambe, K. Yamamoto. Nanoscale Adv. **7**, *1*, 346 (2025). https://doi.org/10.1039/D4NA00740A
[4] D. Chauhan, A. Pujari, G. Zhang, K. Dasgupta, V.N. Shanov, M.J. Schulz. Catalysts **12**, *3*, 287 (2022). https://doi.org/10.3390/catal12030287
[5] E. Thauer, A. Ottmann, P. Schneider, L. Möller, L. Deeg, R. Zeus, F. Wilhelmi, L. Schlestein, C. Neef, R. Ghunaim, M. Gellesch, C. Nowka, M. Scholz, M. Haft, S. Wurmehl, K. Wenelska, E. Mijowska, A. Kapoor, A. Bajpai, S. Hampel, R. Klingeler. Molecules **25**, *5*, 1064 (2020). https://doi.org/10.3390/molecules25051064
[6] X. Gui, J. Wei, K. Wang, W. Wang, R. Lv, J. Chang, F. Kang, J. Gu, D. Wu. Mater. Res. Bull. **43**, *12*, 3441 (2008). https://doi.org/10.1016/j.materresbull.2008.01.028
[7] A. Nagata, H. Sato, Y. Matsui, T. Kaneko, Y. Fujiwara. Vacuum **87**, 182 (2013). https://doi.org/10.1016/j.vacuum.2012.03.008
[8] V. Reguero, B. Alemán, B. Mas, J.J. Vilatela. Chem. Mater. **26**, *11*, 3550 (2014). https://doi.org/10.1021/cm501187x
[9] I. Gómez-Palos, M. Vazquez-Pufleau, R.S. Schäufele, A. Mikhalchan, A. Pendashteh, Á. Ridruejo, J.J. Vilatela. Nanoscale **15**, *13*, 6052 (2023). https://doi.org/10.1039/D3NR00289F
[10] D.R. Tallant, T.A. Friedmann, N.A. Missert, M.P. Siegal, J.P. Sullivan. MRS Proc. **498**, *1*, 37 (1997). https://doi.org/10.1557/PROC-498-37
[11] G.I. Frolov, O.I. Bachina, M.M. Zav'yalova, S.I. Ravochkin. Tech. Phys. **53**, *8*, 1059 (2008). https://doi.org/10.1134/S1063784208080136
[12] M. Vazquez-Pufleau, R.F. Torres, L. Arevalo, N. Abomailek, J.J. Vilatela. Carbon Trends **15**, 100355 (2024). https://doi.org/10.1016/j.cartre.2024.100355
[13] E. Lima, A.L. Brandl, A.D. Arelaro, G.F. Goya. J. Appl. Phys. **99**, *8*, 083908 (2006). https://doi.org/10.1063/1.2191471
[14] T. Ibusuki, S. Kojima, O. Kitakami, Y. Shimada. IEEE Trans. Magn. **37**, *4*, 2223 (2001). https://doi.org/10.1109/20.951130

Translated by M.Verenikina